METRICA
METRology Institutional CAtalog

ISTITUTO NAZIONALE DI RICERCA METROLOGICA
Repository Istituzionale

Quantitative analysis of current–voltage–temperature characteristics of metal-oxide nanowires

Original
Quantitative analysis of current–voltage–temperature characteristics of metal-oxide nanowires / De Carlo, I., Cipollini, D., Fretto, M., Boarino, L., Lamberti, A., Milano, G.. - In: JOURNAL OF PHYSICS D. APPLIED PHYSICS. - ISSN 0022-3727. - 59:43(2026). [10.1088/1361-6463/aeb6ff]

Availability:
This version is available at: 11696/90659 since: 2026-11-03T11:10:17Z

Publisher:
IOP

Published
DOI:10.1088/1361-6463/aeb6ff

Terms of use:

This article is made available under terms and conditions as specified in the corresponding bibliographic description in the repository

Publisher copyright

(Article begins on next page)

27 November 2026

Journal of Physics D:
Applied Physics

PURPOSE-LED PUBLISHING™

PAPER • OPEN ACCESS

Quantitative analysis of current–voltage–temperature characteristics of metal-oxide nanowires

To cite this article: Ivan De Carlo *et al* 2026 *J. Phys. D: Appl. Phys.* **59** 435105

View the article online for updates and enhancements.

You may also like

- Junction properties of single ZnO nanowires with asymmetrical Pt and Cu contacts
Gianluca Milano, Luca Boarino and Carlo Ricciardi
- Thermal fluctuation-induced tunneling conduction through metal nanowire contacts
Yong-Han Lin, Shao-Pin Chiu and Juhn-Jong Lin
- Electron channeling in TiO_2 coated Cu layers
Pengyuan Zheng, Tianji Zhou and Daniel Gall

This content was downloaded from IP address 79.15.22.178 on 30/10/2026 at 09:32

Journal of Physics D: Applied Physics

Check for updates

OPEN ACCESS

RECEIVED
27 January 2026

REVISED
13 October 2026

ACCEPTED FOR PUBLICATION
20 October 2026

PUBLISHED
30 October 2026

Original content from this work may be used under the terms of the Creative Commons Attribution 4.0 licence.

Any further distribution of this work must maintain attribution to the author(s) and the title of the work, journal citation and DOI.

PAPER

Quantitative analysis of current–voltage–temperature characteristics of metal-oxide nanowires

Ivan De Carlo[1], Davide Cipollini[1], Matteo Fretto[1], Luca Boarino[1], Andrea Lamberti[2] and Gianluca Milano[1,2,*]

[1] Advanced Materials Metrology and Life Sciences Division, INRiM (Istituto Nazionale di Ricerca Metrologica), Strada delle Cacce 91, 10135 Torino, Italy

[2] Department of Applied Science and Technology, Politecnico di Torino, C.so Duca degli Abruzzi 24, 10129 Torino, Italy

[*] Author to whom any correspondence should be addressed.

E-mail: g.milano@inrim.it

Keywords: nanowires, single nanowire device, electronic transport in nanowires, metal-semiconductor-metal model, CuO nanowires

Abstract

Electrical transport in single nanowire (NW) devices arises from the interplay between intrinsic conduction properties of the NW and the transport characteristics of metal-semiconductor contact interfaces. Here, we present a framework for the quantitative analysis of current–voltage–temperature (I–V–T) characteristics of metal-oxide NWs. By analyzing experimental data obtained from a nanodevice based on a single CuO NW contacted by metal electrodes, we show that single-NW devices can be described using a metal–semiconductor–metal (M–S–M) transport model that accounts for thermionic emission and thermionic-field emission at Schottky metal-semiconductor interfaces. Through numerical implementation, we show that the M–S–M model distinguishes the electrical transport contributions of the NW from those of the two metal-semiconductor interfaces, enabling the extraction of the temperature-dependent NW resistance and activation energy. The effective interface parameters further provide qualitative insight into the non-ideal contact transport. Comparison with the commonly used large-bias approximation allows us to assess the validity and limitations of this simplified extraction method, while providing an independent cross-check of the quality of the M–S–M transport model. Overall, the proposed approach provides a general framework for disentangling intrinsic NW conduction from contact effects in temperature-dependent two-terminal measurements of single-NW semiconductor devices.

1. Introduction

Semiconductor nanowires (NWs) represent fundamental building blocks for quasi-one-dimensional electronic devices [1, 2]. In particular, metal-oxide NWs have been widely exploited in a broad range of applications, including nanosensors for the detection of chemical [3, 4] and biological species [5], and Schottky-contacted sensing platforms [6]. They have also been employed in NW-based transistors, including general metal-oxide NW transistor architectures [7], depletion-mode ZnO NW field-effect transistors [8], ZnO NW transistors with oxygen-sensing functionality [9], and transparent metal-oxide NW transistors [10]. In the field of resistive switching, metal-oxide NWs have been reviewed as building blocks for memristive devices [11], experimentally demonstrated in multifunctional single-NW systems [12], and investigated as platforms for neuromorphic functionalities [13]. For these applications, single-NW devices are typically fabricated by contacting individual nanostructures with metal electrodes, forming a metal–semiconductor–metal (M–S–M) structure. In addition to the intrinsic semiconductor properties of the nanostructure, the electronic transport characteristics of these devices are regulated by metal–semiconductor (M–S) interfaces, which play a crucial role in determining device performance and functionality. While nearly ohmic contacts are generally preferred for probing the intrinsic electronic properties of NWs [14], rectifying Schottky barriers are essential for enhancing the sensitivity of NW-based sensors [15] and for realizing Schottky-gated biosensing architectures [16] and for

© 2026 The Author(s). Published by IOP Publishing Ltd

enabling NW-based resistive switching devices through control of the metal–nanowire interfaces [17], including devices with asymmetric metal contacts [18]. Previous studies have reported quantitative analyses of experimental current–voltage characteristics measured at room temperature. Liu *et al* developed a procedure for fitting nonlinear characteristics and retrieving transport parameters in semiconducting nanostructures [19], while Zhang *et al* described the numerical treatment of back-to-back Schottky-junction devices [20]. However, a quantitative analysis of current–voltage characteristics over a broad temperature range, capable of disentangling NW and contact contributions, is still lacking. In particular, there is a need to combine behavioral descriptions with theoretical-based modeling, in order to extract fundamental physical parameters that govern the operation of single-NW devices contacted by metallic electrodes.

In this work, we present a framework for the quantitative analysis of current–voltage–temperature (I–V–T) characteristics of metal-oxide NWs, using two-terminal devices based on individual CuO NWs as a representative system. The main advantage of the M–S–M model is its ability to separate the voltage and transport contributions of the NW from those of the two M–S interfaces. This enables the extraction of the intrinsic NW resistance as a function of temperature and, consequently, the evaluation of the activation energy associated with NW conduction. The extracted resistance is compared with that obtained using the large-bias approximation, which is commonly employed in the literature, providing a consistency cross-check of the proposed approach and allowing the limitations of the approximation to be assessed. In addition, the model provides effective interface parameters, including the ideality factors of the two junctions, which offer qualitative insight into the non-ideal transport mechanisms governing the M–S contacts. Overall, this framework provides a practical route to disentangle intrinsic NW electrical transport from interface effects in two-terminal measurements, enabling a more reliable interpretation of single-NW devices in which non-ideal M–S interfaces play a central role.

2. Theoretical background

2.1. The M–S model

Single NW-based devices usually consists in a semiconductor NW contacted by two metal electrodes. The scanning electron microscopy (SEM) image of the device based on a CuO NW investigated in this work is shown in figure 1(a). Rather than forming ideal ohmic contacts, M–S interfaces typically exhibit non-linear I–V characteristics due to the presence of Schottky barriers [21–23]. Carrier transport across a Schottky interface is primarily determined by the width and shape of the depletion region rather than by the overall dimensions of the device. When the depletion region is sufficiently wide, charge transport is predominantly governed by thermionic emission (TE), and the reverse current is often approximated by its saturation value. Conversely, when the depletion region becomes sufficiently narrow as a result of the carrier concentration, interface electrostatics, or the applied electric field, tunneling through the barrier becomes non-negligible and thermionic-field emission (TFE) must be considered. In the present devices, the CuO NW extends over a micrometre-scale distance between the electrodes, whereas charge injection occurs across nanometre-scale depletion regions at the M–S interfaces. Therefore, the distinction between TE and TFE regimes refers to the characteristic width of the interfacial barrier and the associated transport mechanism. This description follows the classical treatments of carrier transport through Schottky barriers developed by Padovani and Stratton [21] and by Crowell and Rideout [24].

Electrical transport in single NW-based devices can be modeled following the approach described in [19, 20]. The two M–S interfaces are represented as the two Schottky diodes connected back-to-back, as schematically shown in figure 1(b). Each diode includes a shunt resistance (R_{sh}) connected in parallel to account for leakage current across the junction, which mainly affects low-bias conduction. A series resistance R_{NW} describes the nearly ohmic transport through the micrometer-scale NW connecting the two diodes. Assuming a sufficiently large band gap between the valence and the conduction bands, the model introduced in [20, 21] adopts a single-band effective-mass equation for each M–S interface. Under forward bias, TE dominates over field assisted transport mechanism and it is therefore assumed to sufficiently describe carrier emission across the Schottky junction. The corresponding current density equation is given by [20, 23]:

$$J_f(V) = A^* T^2 e^{-\frac{q\Phi}{k_B T}} e^{\frac{qV}{\eta k_B T}} \left(1 - e^{-\frac{qV}{k_B T}}\right) \quad (1)$$

where Φ is the effective Schottky barrier height of the diode on the right in figure 1, k_B is the Boltzmann constant, q is the elementary charge, T is the absolute temperature, and η is the

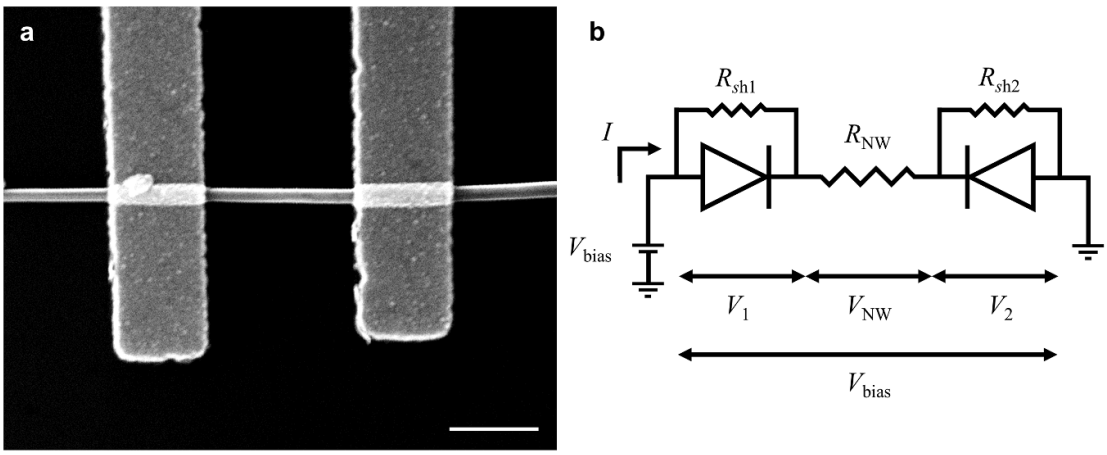


Figure 1. (a) SEM image of the single CuO NW device contacted by Cu contacts (scale bar, 500 nm). (b) Equivalent circuit of the Metal—Metal Oxide NW—Metal and its schematic diagram described by a semiconducting NW connected to two back-to-back Schottky diodes.

dimensionless ideality factor, which quantifies deviations from ideal diode behavior ($\eta = 1$). The quantity $A^* = 4\pi m^* q k_B^2/h^3$ is the semiconductor Richardson's constant, with m^* denoting the effective mass of the dominant charge carrier. When the depletion region of a reverse-biased Schottky junction is sufficiently narrow, field-assisted tunneling can contribute significantly to carrier transport and cannot be neglected. This contribution can be described within the TFE framework [20, 21], yielding the following expression for the reverse current density:

$$J_r(V) = \frac{A^* T}{k_B}\sqrt{\pi E_{00}}\left(q(V-\xi) + \frac{q\Phi}{\cosh^2(E_{00}/k_B T)}\right)^{\frac{1}{2}} e^{-\frac{q\Phi}{E_0}}\, e^{qV\left(\frac{1}{k_B T}-\frac{1}{E_0}\right)} \tag{2}$$

where ξ denotes the energy separation between the Fermi level and the bottom of the conduction band for n-type semiconductors (or the top of the valence band for p-type materials, as is the case of CuO NWs). Equation (2) can be rewritten as $J_r = J_s e^{qV\left(\frac{1}{k_B T}-\frac{1}{E_0}\right)}$, where $J_s(V,T)$ collects the prefactors of the TFE current. In particular, J_s exhibits a square-root dependence on the applied voltage, which varies more slowly than the exponential term over the investigated voltage range. The voltage dependence of the reverse current is therefore mainly governed by the exponential contribution, whose characteristic energy E_0 is related to E_{00} through

$$E_0 = E_{00}\coth\left(\frac{E_{00}}{k_B T}\right), \qquad E_{00} = \frac{\hbar q}{2}\sqrt{\frac{N_D}{m^*\epsilon_s\epsilon_0}}. \tag{3}$$

Here, N_D is the carrier density at the interface, while ϵ_s and ϵ_0 are the relative permittivity of the NW and the vacuum permittivity, respectively. The parameter E_{00} defines the characteristic energy scale governing the crossover between TE and field-assisted tunneling at the Schottky barrier. Specifically, it corresponds to the diffusion potential for which a carrier at the edge of the depletion region has a tunneling transmission probability equal to $1/e$.

When $E_{00} \sim k_B T$, transport is mainly governed by TFE, whereas for $E_{00} \gg k_B T$ TE becomes negligible and charge transport occurs mainly via tunneling. Conversely, for $E_{00} \ll k_B T$, transport is dominated by TE. The interested reader is referred to figure 3 of [21] for further details. Imposing local charge conservation ($I = I_1 = I_{NW} = I_2$) and applying Kirchhoff's voltage law ($V = V_1 + V_{NW} + V_2$), the system of equations describing the device reads:

$$\begin{cases} S_1 J_1(V_1) + V_1/R_{sh} = (V - V_1 - V_2)/R_{NW} \\ S_2 J_2(V_2) + V_2/R_{sh} = (V - V_1 - V_2)/R_{NW} \end{cases} \tag{4}$$

where J_1 and J_2 correspond to either J_r or J_f, depending on the bias polarity of each junction. This system does not admit a closed form analytical solution due to the exponential dependence of the current densities, however, it can be efficiently solved using numerical methods.

2.2. Numerical implementation

Equation (4) can be rewritten in compact form as $\vec{F}(V_1, V_2) = 0$, where:

$$\vec{F}(V_1, V_2) = \begin{bmatrix} F_1(V_1, V_2) \\ F_2(V_1, V_2) \end{bmatrix} = \begin{bmatrix} S_1 J_1(V_1) + V_1/R_{sh} - (V - V_1 - V_2)/R_{NW} \\ S_2 J_2(V_2) + V_2/R_{sh} - (V - V_1 - V_2)/R_{NW} \end{bmatrix} \quad (5)$$

$\vec{F}(V_1, V_2)$ is non-linear in $\vec{V} = V_1, V_2$, and an approximate root can be obtained iteratively using numerical root finding methods, such as the Newton–Raphson scheme [19] or Brent's method [25].

Unlike previous works, which solved the problem using the Newton–Raphson method [19, 20], here we adopt Brent's method, as it guarantees convergence without requiring the evaluation of derivatives. This feature is particularly advantageous when dealing with exponential equations, for which Jacobian or derivative computations may lead to numerical instability or poor convergence behavior. Brent's method iteratively refines the interval in which the function changes sign, providing a stable and reliable localization of the root. As a result, it is more robust than derivative based approaches, especially in the presence of strongly non-linear I–V characteristics.

3. Results and discussion

3.1. Single NW-based devices

Copper oxide NWs were grown by thermal annealing, a process based on the sequential oxidation of the Cu substrate, passing from an initial Cu_2O layer, followed by the development of a CuO/Cu_2O bi-layer, and the subsequent Cu diffusion through the grain boundaries, leading to the growth of CuO NWs. This growth mechanism has been widely studied and reported in the literature [26–28]. The structural properties and chemical composition of the CuO NWs have been investigated in detail in a previous work [29]. In brief, the structure of the CuO NWs is characterized by the coexistence of tenorite and cuprite phases, while the stoichiometry has been confirmed to correspond to CuO rather than Cu_2O.

Devices based on single CuO NWs were fabricated by dispersing NWs onto an insulating substrate and subsequently contacting isolated NWs via electron-beam lithography (EBL), metal evaporation, and lift-off to realize two-terminal single NW devices (details in section 5.2) [29]. Using this approach, devices obtained by contacting CuO NWs with Cu and Au electrodes were realized, as shown in figures 2(a) and (b) respectively.

3.2. Quantitative analysis of the effect of contact metals

Realizing devices with different metal contacts enables investigation of the influence of contact metals on the electronic transport properties of single NW devices. Electrical characterization shows that NWs contacted with Au and Cu electrodes exhibit nearly symmetric I–V characteristics. However, devices with Cu contacts reach the large-bias conduction regime at lower applied voltages compared to those with Au contacts, for which a non-negligible current is observed only for applied voltages exceeding ~ 10 V. This behavior is consistent with the response expected from a back-to-back connected Schottky diode configuration with a resistor in series, as described by the M–S–M model. It is worth mentioning that nonlinearities can be mainly ascribed to transport properties at the M–S interface, as pointed out in a previous work where the two-terminal characteristics of contacted CuO NWs were compared with results obtained in four-terminal configuration, where the effect of contact resistance is eliminated [29].

The I–V curves are not perfectly symmetric, reflecting slight differences between the two M–S interfaces. Such asymmetries in nanoscale devices with nominally identical contacts can be attributed to small fluctuations in the contact area, localized defects, residuals of chemical contamination from nanocontact fabrication, and variations in metal grain orientation [17, 30, 31]. However, the M–S–M model is able to describe single NW devices with asymmetric contacts and allows extraction of the parameters associated with each individual interface.

The quantitative effect of metal contacts on the I–V characteristics was evaluated by fitting the experimental data using the M–S–M model. The contact area S was considered as the rectangular overlap region between the electrodes and the CuO NWs, as determined from SEM images, while the effective mass was fixed to $m^* = 0.78\ m_e$ [32]. The fitting parameters were found to be in quantitative agreement with theoretical expectations. In particular, the extracted value of E_{00} remains lower than the thermal energy $k_B T$ over the whole investigated temperature range, indicating that TE remains relevant at both interfaces. Moreover, since E_{00} becomes increasingly comparable to $k_B T$ upon cooling, field-assisted tunneling is expected to progressively augment its contribution to the reverse biased junction. These

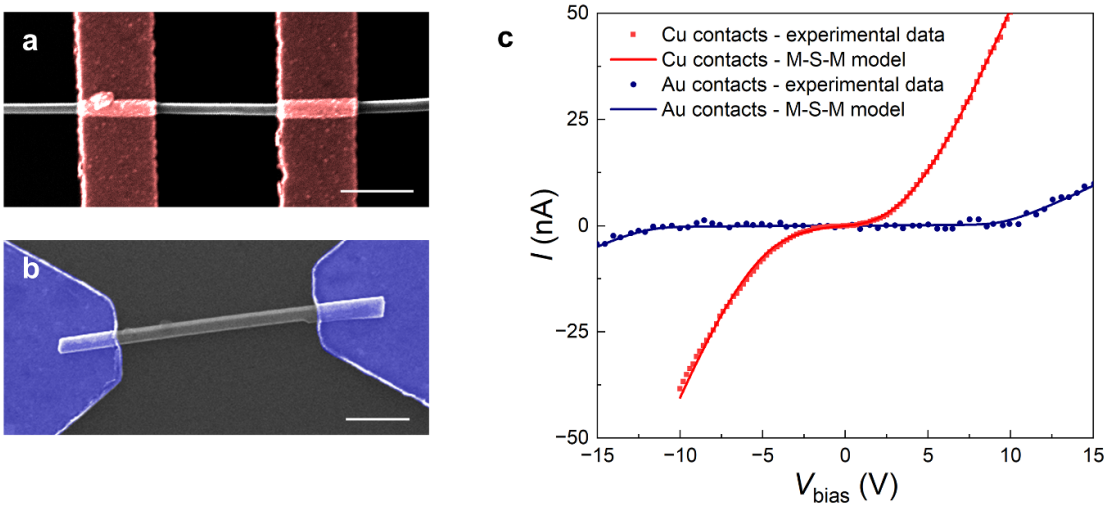


Figure 2. (a), (b) SEM images of the two CuO nanowire devices, in false color, highlighting the different materials of the contacts, red electrodes and blue electrodes for Cu and Au respectively (scale bars, 500 nm). (c) Two terminal *I–V* characteristics of two single CuO nanowire devices with different materials of the metallic contacts: Cu red squares and Au blue circles. The solid lines represent the fitted theoretical curves obtained by the conduction model. The two curves highlight the Schottky barriers between the CuO nanowire and the two different metals, suggesting the choice of Cu for performing the temperature analysis.

results support the use of TE and TFE expressions for the forward and reverse biased junctions, respectively, within the Padovani and Stratton framework [21].

Moreover, the extracted shunt resistance R_{sh} was orders of magnitude larger than the R_{NW} in accordance with the ideal Schottky barrier limit ($R_{sh} \to \infty$).

Measurements were performed at $T = 300$ K in vacuum (details in section 5.3). The experimental characteristics were reproduced using independent effective ideality factors for the two junctions, allowing the model to account for the non-equivalence and non-ideal behavior of the two M–S interfaces. The extracted ideality factors indicate that the contacts deviate substantially from ideal thermionic-emission behavior and should therefore be interpreted as effective interface parameters. For Cu-contacted NWs, the extracted Cu/CuO Schottky barrier height was $\Phi_{Cu/CuO} \approx 0.5$ eV, whereas for Au-contacted devices the barrier height was $\Phi_{Au/CuO} \approx 0.7$ eV [33]. The two devices contain different CuO NWs and exhibit different geometries, particularly in terms of NW diameter and electrode separation. Therefore, identical values of R_{NW} are not expected. To compare the intrinsic NW contributions, the fitted resistances were converted into resistivities using the corresponding NW lengths and cross-sectional areas. The resulting values are $\rho_{Cu\ pads} = (0.527 \pm 0.016)\ \Omega$m for the Cu-contacted device and $\rho_{Au\ pads} = (1.4 \pm 0.3)\ \Omega$m for the Au-contacted device. Although the two values differ by approximately a factor of three, they remain within the same order of magnitude. Such variability is reasonable for individual CuO NWs grown by thermal oxidation, whose transport properties may vary because of differences in geometry, stoichiometry, defect density, microstructure, and surface condition.

Theoretical Schottky barrier heights evaluated from metal work functions, electron affinity and energy gap, predict lower values for Au/CuO interfaces compared to Cu/CuO, in contrast to the experimental observations [12, 33]. This discrepancy can be attributed to interface chemistry effects [34, 35]. In particular, Cu/CuO contacts are more susceptible to oxygen diffusion from the metal-oxide NW into the metal electrodes, leading to barrier lowering through the formation of intermediate interfacial phases. Conversely, the noble metal nature of Au suppresses such effects at the Au/CuO interface [34, 36]. Due to the lower barrier at the M–S interface, electron transport properties of single CuO NW-based devices contacted with Cu electrodes have been exploited in the following for the temperature-dependent analysis.

3.3. Quantitative analysis of *I–V–T* characteristics

3.3.1. Experimental characteristics

Temperature dependent characteristics of a single CuO NW are shown in figure 3(a) (logarithmic scale graph in figure 3(b)). The lower temperature limit of the measurements was determined by the very small currents obtained at low temperatures, which become difficult to measure upon further cooling. The decrease in the current flowing through the device with decreasing temperature can be ascribed to both the intrinsic semiconducting behavior of the metal-oxide NW and the progressive suppression

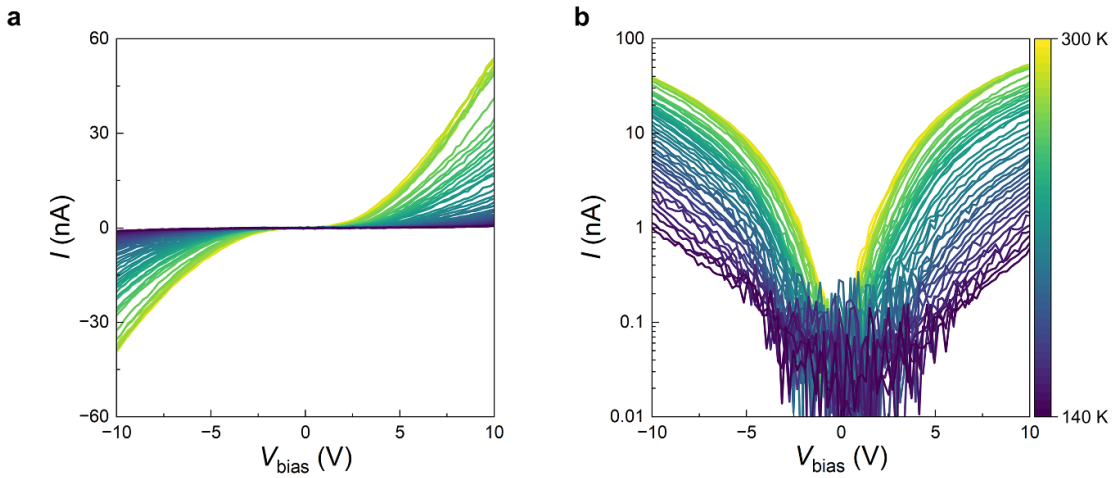


Figure 3. (a) and (b) Experimental *I–V* curves of the single CuO NW performed in 140–300 K temperature range, in linear and log scale respectively.

of charge transport across the Schottky barriers [37, 38]. Accordingly, the large-bias conduction regime shifts toward higher applied voltages as the temperature decreases.

3.3.2. Quantitative analysis

Quantitative analysis of the *I–V–T* characteristics was performed by applying the M–S–M model (see section 5.4 for details). The temperature-independent interface parameters were optimized using the complete set of *I–V–T* characteristics, whereas R_{NW}, η_1, and η_2 were fitted independently at each temperature. This parameterization was defined by combining physical considerations with numerical identifiability. In particular, Φ_1, Φ_2, E_{00}, and ξ were treated as temperature independent because they mainly describe structural and electrostatic properties of the metal-NW interfaces, which are not expected to vary substantially over the investigated temperature range. Optimizing these parameters over the complete *I–V–T* dataset also reduces parameter correlations and improves the stability of the fitting procedure. By contrast, R_{NW} was allowed to vary with temperature to describe the temperature-dependent conduction of the NW, while η_1 and η_2 were treated as temperature-dependent effective parameters that account for non-ideal carrier injection and may incorporate temperature-dependent interface effects. The model was found to accurately reproduce the experimental data over the entire investigated temperature range. Representative fits of *I–V* characteristics at three temperatures (300 K, 210 K and 140 K) are shown in figures 4(a)–(c). In this case, quantitative analysis enables the evaluation of the voltage drop across the two M–S interfaces and the NW according to:

$$V_{NW} = V_{bias} - V_1 - V_2 \tag{6}$$

where V_1 and V_2 denote the voltage drops at the M–S interface 1 and 2, respectively, as schematically illustrated in figure 1(b). The voltage drop across each element of the single NW device as a function of the applied bias voltage (V_{bias}) at the three representative temperatures is reported in figures 4(d)–(f). The voltage drops V_1 and V_2 exhibit different trends depending on the applied-bias polarity, reflecting the interchange of the forward- and reverse-biased roles of the two junctions, as shown in figures 4(d)–(f). Owing to the electrical non-equivalence of the two interfaces, the applied voltage is not distributed symmetrically between them [31]. Moreover, because the effective ideality factors differ substantially from unity, the voltage drop across the forward-biased junction is not negligible. This contribution becomes increasingly relevant upon decreasing temperature, as shown by comparing figure 4(d)–(f), when carrier injection across both interfaces is progressively suppressed. Therefore, the total contact contribution includes finite voltage drops across both the reverse- and forward-biased junctions, particularly at the lowest investigated temperature shown in figure 4(f). At low applied bias, most of the voltage drops across the two M–S interfaces and V_{NW} remains comparatively small. As the applied bias increases, the fraction of voltage dropping along the NW increases. Nevertheless, comparison of figure 4(d)–(f) shows that, upon decreasing temperature, an increasing fraction of the applied voltage is sustained by the interfaces, including a non-negligible contribution from the forward-biased junction. This behavior highlights the importance of explicitly accounting for both junctions when separating the NW and contact contributions.

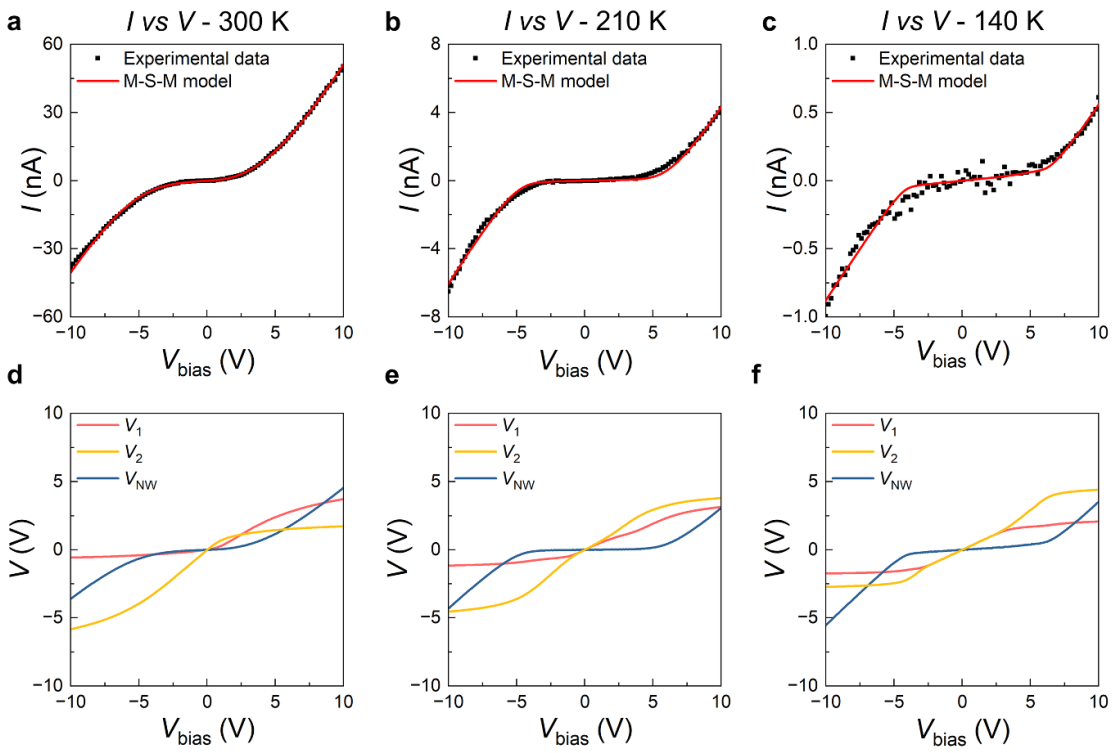


Figure 4. (a)–(c) Experimental *I*–*V* curves of the single CuO NW device at three different temperatures and their theoretical fit, represented respectively by black squares and solid red lines. (d)–(f) Voltage bias dependence of the voltage drops at different temperatures of the two Schottky diodes (red and yellow lines) and of the CuO NW (blue line), extrapolated by the numerical solving of the equation system 4 for the fitting of the curves reported in (a)–(c).

3.3.3. NW resistance

In the following section, we compare the NW resistance extracted from the M–S–M model with that obtained using the large-bias approximation. This approximation is commonly adopted in the literature for rapid estimation of the NW resistance, neglecting the physical contribution of other circuit elements [39–43]. In case of large-bias approximation, the NW resistance is evaluated through the relationship $R_{\mathrm{NW}} \approx \frac{\mathrm{d}V}{\mathrm{d}I}|_{\mathrm{large-bias}}$. However, identifying the appropriate large-bias regime is nontrivial without *a priori* knowledge of the actual contribution of the NW resistance to the overall transport behavior of the device. For this purpose, we evaluated the voltage-drop profiles across the M–S interfaces and the NW as a function of temperature, using experimental data within the M–S–M model. Figure 5 shows the temperature dependence of the normalized voltage drop across the two interfaces and the NW for three selected V_{bias} (5 V, 8 V, and 10 V). Both the voltage drop of the reverse-polarized diodes and the forward-biased diodes are shown over the entire investigated temperature range.

According to the principle underlying the large-bias approximation, at a fixed temperature a larger V_{bias} results in a larger fraction of the voltage drop occurring across the NW. However, upon decreasing temperature, even the largest V_{bias} becomes insufficient to prevent the Schottky diodes from dominating the voltage partitioning, indicating that only a small fraction of V_{bias} drops across the metal-oxide NW. It turns out that the large-bias approximation becomes increasingly less accurate as the temperature decreases, since the voltage drop becomes progressively less dependent on the NW itself.

Figure 6(a) reports the R_{NW} obtained using both the M–S–M model and the large-bias approximation. In the latter case, the resistance was evaluated by linearly fitting the experimental data in the voltage range 8–10 V. As expected from a semiconducting material, the resistance increases monotonically with decreasing temperature. The M–S–M resistance is systematically lower than the large-bias estimate over the investigated temperature range. This difference is physically expected because the large-bias approximation assigns the entire differential voltage drop to the NW, although a finite contribution from the two M–S contacts remains. The large-bias value should therefore be regarded as an effective two-terminal resistance, whereas the M–S–M model explicitly separates the interface and NW voltage

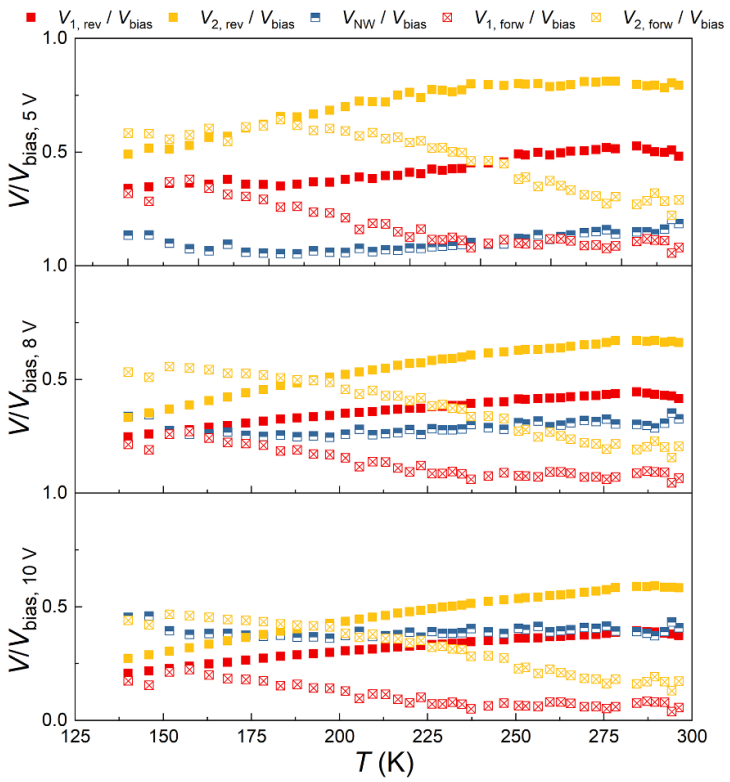


Figure 5. Temperature dependence of the normalized voltage drops of the two Schottky diodes and of the CuO NW, evaluated at different voltage bias: 5 V, 8 V and 10 V. Both reverse and forward biased diode contributions have been reported.

contributions. The difference between the two estimates increases upon decreasing temperature, consistently with the progressively larger fraction of the applied voltage sustained by the M–S interfaces. The advantage of the M–S–M analysis is therefore not merely the extraction of another resistance value, but the ability to distinguish the NW contribution from the residual contact contribution.

3.3.4. Activation energy

Semiconducting electronic transport is commonly associated with a thermally activated conduction mechanism [44, 45]. In this context, the extrapolation of the activation energy governing transport properties of the NW, E_A, is crucial for understanding the conduction behavior of such nanostructures [14, 46, 47]. A thermally activated conduction mechanism can be described by the Arrhenius relation:

$$\sigma = \sigma_0 \, e^{-\frac{E_A}{k_B T}} \tag{7}$$

where σ is the electrical conductivity, and σ_0 its conductivity at 0 K, E_A is the activation energy and $k_B T$ is the thermal energy. E_A can be estimated from the slope of the Arrhenius plot of $\ln(\sigma)$ as a function of $10^3/T$.

In case of CuO NWs, which are intrinsic p-type semiconductors [29, 32], their electrical transport is mainly governed by holes, and E_A can be associated with their hopping type conduction mechanism [48, 49]. The electrical conductivities obtained from the R_{NW} extracted using the M–S–M model and the large-bias approximation are reported in figure 6(b) as a function of $10^3/T$. The logarithmic scale highlights that the two methods provide clearly different absolute conductivity values over the complete investigated temperature range. In particular, the difference remains appreciable even near room temperature, although it appears less evident when the corresponding resistance values are displayed on a linear scale in figure 6(a).

Despite their different absolute conductivity values, the two datasets exhibit similar temperature dependencies, as shown in figure 6(b). By modeling conduction as an Arrhenius type in the higher temperature regime, linear fits in the 200–300 K range yield activation energies of $E_{A,M-S-M} = (133 \pm 3)$ meV for the M–S–M analysis and $E_{A,LB} = (138 \pm 2)$ meV for the large-bias approximation. Thus, the large-bias approximation provides a comparable estimate of the effective activation energy within this temperature interval, although it systematically underestimates the NW conductivity. Note that, however,

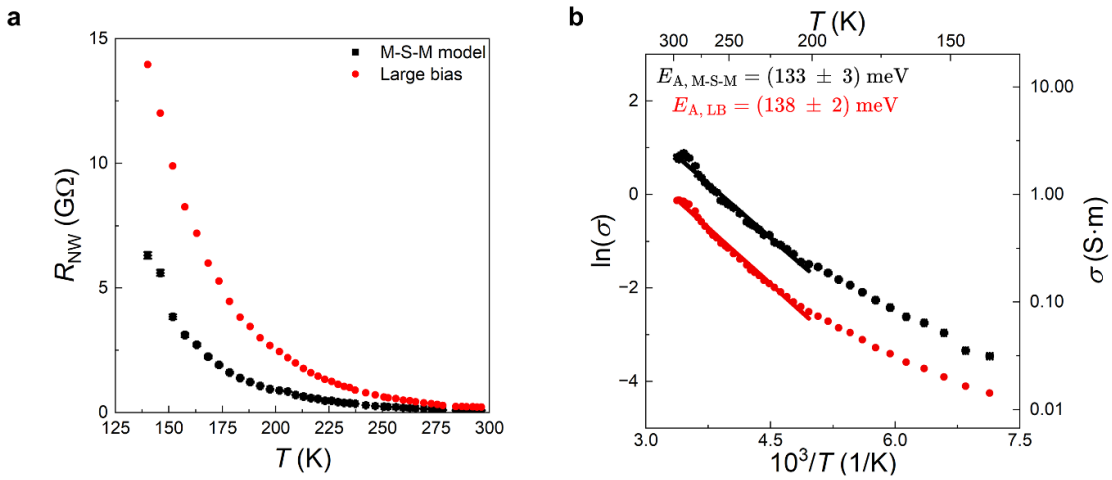


Figure 6. (a) Temperature dependence of the CuO nanowire resistance extracted using the M–S–M model (black squares) and the large-bias linear approximation (red circles). The R_{NW} obtained from the M–S–M model is systematically lower, over the entire investigated temperature range, to the large-bias estimation. This difference arises because the large-bias approximation still contains a residual contribution from the two Schottky contacts, whereas the M–S–M model separates the voltage drops across the metal–semiconductor interfaces from that along the nanowire. (b) Arrhenius plot of the electrical conductivity calculated from the two resistance estimates. Although the absolute conductivity values differ, the two datasets exhibit comparable temperature dependence and yield mutually compatible activation energies from the slope of the linear fit of $ln(\sigma) - 10^3/T$.

the complete dataset cannot be described by a single Arrhenius slope in the whole temperature range, and deviations from linear behavior reflect the non-negligible contributions of different conduction mechanisms.

It is worth mentioning that the obtained values of E_A are in qualitative accordance with values reported in the literature. For example, E_A evaluated in a single CuO NW grown by thermal annealing and contacted in four-terminal configuration has been observed to be $E_A = 118$ meV [50]. Higher activation energies have been reported when the NW resistance was extracted in the low-bias regime, such as ($E_A = 327$ meV in [30] and $E_A = 272$ meV in [51]). In these cases, these higher values are likely influenced by the specific bias conditions used to evaluate the R_{NW}. More evident deviations from ideal linear Arrhenius behavior may be visible at the lowest investigated temperatures. Although the slight nonlinearity of the Arrhenius plot may warrant further investigation using more specific transport models, a detailed assessment of possible variations in the activation energy or conduction mechanisms is left for future work, as it lies beyond the scope of the present study.

3.3.5. M–S Interface parameters

In the discussed fitting procedure, the effective Schottky barrier heights Φ_1 and Φ_2, the characteristic tunneling energy E_{00} and the effective Fermi-level offset ξ are optimized over the whole temperature-dependent dataset, as discussed in section 5.4. This assumption reduces the large uncertainties, reducing the number of independently fitted quantities relative to the number of experimental data points, improving convergence, and decreasing the uncertainty in R_{NW}, particularly at low temperatures. The resulting values are reported in table 1. The two effective Schottky barrier heights are comparable, although not identical. Their similar magnitude is consistent with the approximately symmetric shape of the measured *I–V* characteristics, whereas their finite difference reflects the electrical non-equivalence of the two nominally similar Cu/CuO interfaces. Moreover, these are comparable in magnitude to values reported for semiconducting NW devices analyses using back-to-back Schottky-junction models within the TFE framework [19, 20]. At the nanoscale, small variations in contact area, local morphology, interfacial contamination, defect density, and barrier inhomogeneity can produce measurable differences between the two junctions, as demonstrated by the correlation between contact geometry and local potential profiles reported by Bercu *et al* [31].

The characteristic tunneling energy E_{00} determines the relative importance of TE and field-assisted transport at the Schottky interfaces. The extracted value, $E_{00} = 6.7$ meV, remains lower than k_BT over the investigated temperature range, although the two energy scales become increasingly comparable upon cooling. This result indicates that TE remains relevant throughout the investigated range, while TFE becomes progressively more important at lower temperatures.

Table 1. Temperature-independent parameters obtained from the M–S–M fitting procedure. The reported uncertainties correspond to the standard errors estimated from the covariance matrix of the fit.

Parameter	Fitting value
Φ_1 (eV)	0.433 ± 0.018
Φ_2 (eV)	0.494 ± 0.009
E_{00} (eV)	0.0067 ± 0.0002
ξ (eV)	0.2 ± 1.9

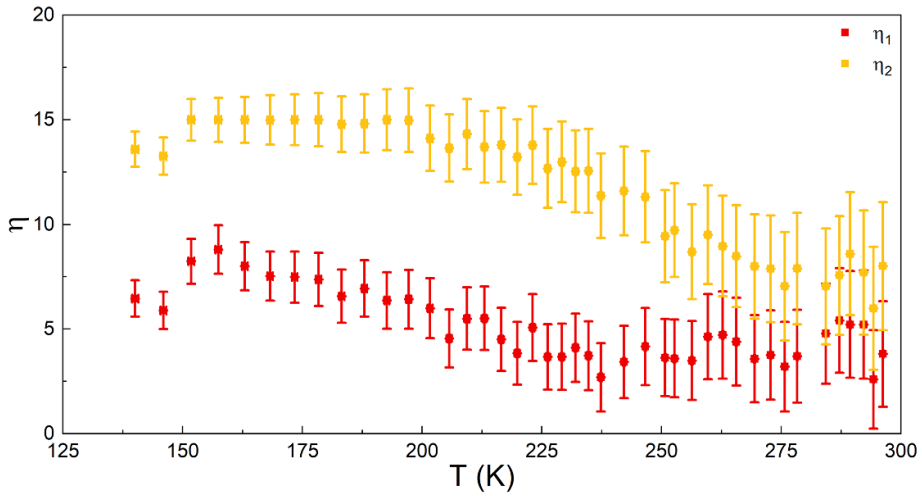


Figure 7. Temperature dependence of ideality factor of the two Schottky junctions.

The fitted value of ξ is associated with an uncertainty substantially larger than the parameter itself. This demonstrates that ξ is only weakly constrained by the present two-terminal electrical measurements, owing to its comparatively weak contribution to the TFE expression and to its correlation with the other interface parameters. Therefore, ξ should be regarded as an effective temperature-independent fitting parameter, and no precise physical conclusion regarding the Fermi-level position can be drawn from its fitted value.

Unlike the temperature-independent parameters reported in table 1, the effective ideality factors η_1 and η_2 are allowed to vary independently with temperature. Their temperature dependence is reported in figure 7. Both ideality factors are substantially larger than the ideal value $\eta = 1$, showing that carrier injection at the two interfaces cannot be described by ideal TE alone. The extracted values should therefore be interpreted as effective parameters accounting for several non-ideal interface contributions, including barrier inhomogeneity, interface states, trap-assisted transport, tunneling, possible interfacial layers, and local contact asymmetry. The two ideality factors exhibit different values and temperature dependences, providing further evidence that the two Cu/CuO contacts are not electrically equivalent. Nevertheless, both follow physically consistent trends and remain within comparable ranges over the complete temperature interval. A similar temperature dependence of the ideality factor has been reported both for CuO-based Schottky diodes by Jana *et al* [52] and for single semiconducting NW Schottky junctions by Jin *et al* [53], with η increasing upon cooling, a trend commonly associated with non-ideal transport and spatial inhomogeneity of the M–S barrier. These results support the use of separate temperature-dependent ideality factors for the two junctions rather than imposing identical or near-ideal values.

4. Conclusions

In summary, this work demonstrates the use of an M–S–M model for separating the NW and interface contributions to the temperature-dependent electrical response of single-NW devices. Using a CuO NW device as a representative system, the model reproduces the measured *I–V–T* characteristics across a wide

range of temperatures. This separation enables the investigation of the intrinsic electrical transport properties of the semiconducting NW itself, through the voltage partitioning across the single-NW device. The NW resistance extracted from the M–S–M analysis is systematically lower than that obtained using the commonly adopted large-bias approximation, showing that a residual contact contribution remains even at high applied bias. Nevertheless, the two approaches yield mutually compatible activation energies, indicating that the large-bias approximation captures the dominant thermally activated energy scale while providing less accurate absolute resistance.

The analysis also provides effective parameters describing the two M–S interfaces. Their values and temperature dependencies indicate non-ideal and electrically non-identical contacts, while their interpretation remains subject to parameter correlations and to the sensitivity of two-terminal electrical measurements. In particular, the effective ideality factors provide qualitative information on non-ideal interface transport rather than a direct identification of individual microscopic mechanisms.

Overall, the proposed framework provides a practical route for disentangling intrinsic NW conduction from contact effects in two-terminal I–V–T measurements. It therefore supports a reliable interpretation of single-NW semiconductor devices in which non-ideal M–S interfaces provide a non-negligible contribution to the measured electrical response.

5. Materials and methods

5.1. NW growth

CuO NWs were grown via thermal annealing of a Cu foil (30 μm thick, 99.9% purity). After removal of the native CuO_x layer by immersion in an aqueous HCl solution (1 M) for 2 min, the Cu samples were annealed in a convection oven under ambient atmosphere at a temperature of 430 °C. The annealing process leads to the formation of an initial Cu_2O layer, followed by a second layer of CuO on the top of it, and finally the growth of the CuO NWs takes place [26, 29, 54].

5.2. Single NW device fabrication

Single CuO NW devices were realized using EBL and metal evaporation [29]. First, CuO NWs were randomly dispersed onto a pre-patterned silicon substrate with a thermally grown silicon dioxide layer, featuring Ti/Au (5/200 nm) contact tracks fabricated by laser lithography and sputter deposition. NWs dispersion was assisted by gentle mechanical scratching in proximity to the electrode edges. An ad hoc contact layout was then designed for EBL, which was performed on a PMMA layer spin-coated on the substrate. Finally, metal contacts (Cu or Au) were deposited by e-beam evaporation under high-vacuum conditions, followed by lift-off in acetone and ethanol baths.

5.3. Electrical characterization

Electrical characterization was carried out inside a two-stage cryocooler (Leybold ROK 10-300). The sample was thermally anchored to the cryocooler cold finger inside of the vacuum chamber evacuated to a base pressure of 10^{-5} mbar, enabling controlled temperature variation. A gradual temperature increase was obtained by switching off the cryocooler, allowing passive self-heating of the devices up to room temperature. Temperature was measured using a silicon diode sensor (LakeShore DT-670) controlled by a LakeShore 331 temperature controller. I–V characteristics in the voltage range $\pm$10/10 V were acquired between 300 K and 140 K, with a temperature step of around 1 K, using a Keithley 6430 Sub-Femtoamp SourceMeter, employed for both voltage sourcing and current reading and remotely controlled via Python code.

5.4. Fitting of experimental data

The experimental I–V characteristics were analyses using the M–S–M model described in section 2.1. For each applied bias, temperature, and trial parameter set, the nonlinear system defined in equation (5) was solved numerically to obtain the voltage drops V_1 and V_2 across the two M–S interfaces. The voltage drop across the NW and the corresponding device current were then calculated as $V_{NW} = V_{bias} - V_1 - V_2$ and $I = V_{NW}/R_{NW}$, respectively. The numerical procedure was implemented in Python using the SciPy library [55]. Brent's method was used to solve the nonlinear equations at each value of V_{bias}, while the model parameters were determined by nonlinear least-squares fitting of the simulated characteristics to the experimental data. The numerical tolerance and maximum number of iterations were set to 10^{-12} and 10^3, respectively. The fitting parameters were divided into fixed, temperature-independent and dependent quantities. The shunt resistance R_{sh} was estimated from the linear low-bias region of each experimental I–V characteristic and kept fixed during the optimization. The effective Schottky barrier

heights Φ_1 and Φ_2, the characteristic tunneling energy E_{00}, and the effective Fermi-level offset ξ were treated as temperature-independent parameters fitted using the whole dataset of I–V–T curves. The NW resistance $R_{NW}(T)$ and the ideality factors $\eta_1(T)$ and $\eta_2(T)$ were independently optimized at each temperature. The optimization was performed in two stages. First, $R_{NW}(T)$ was fixed to the value estimated from the linear large-bias region, while the remaining parameters were optimized. The resulting values were then used as initial estimates for a second fit in which $R_{NW}(T)$ was also allowed to vary. Parameter uncertainties were estimated from the covariance matrix of the nonlinear least-squares fit, calculated from the Jacobian of the residual vector. The reported uncertainties correspond to one standard deviation (1σ). The NW resistance extracted using the large-bias approximation was determined from the slope of the linear fit of the I–V characteristics in the voltage interval 8–10 V; the associated uncertainty was derived from the standard error of the least-squares fit. The activation energy (E_A) was evaluated by performing a linear fit of $\ln(\sigma)$ as a function of $10^3/T$. The uncertainty in E_A was obtained from the fit parameters, however, the regression was unweighted and therefore did not explicitly account for the uncertainties resulted from the large-bias and M–S–M model evaluations of σ.

Acknowledgement

G.M. acknowledges support by the European Research Council (ERC) under the European Union's ERC Starting Grant (ERC-2024-STG) agreement MEMBRAIN No. 101160604. Views and opinions expressed are however those of the authors only and do not necessarily reflect those of the European Union or the European Research Council. Neither the European Union nor the granting authority can be held responsible for them. Part of this work was supported by the European project 24GRD09 Hymetbat. The project has received funding from the European Partnership on Metrology, cofinanced from the European Union's Horizon Europe Research and Innovation Programme, and by Participating States. Part of this work has been carried out at Nanofacility Piemonte INRiM, a laboratory supported by the 'Compagnia di San Paolo' Foundation, and at the QR Laboratories, INRiM, a micro and nanofabrication lab.

Data availability statement

The data that support the findings of this study are openly available at the following URL/DOI: https://doi.org/10.5281/zenodo.23 214 676 [56].

Code availability

The codes used to generate datasets of simulations can be accessed on GitHub (https://github.com/IvanDeCarlo-PhD/Quantitative-analysis-of-I-V-T-characteristics-of-MetalOxide-NWs). The code release is available on Zenodo (https://doi.org/10.5281/zenodo.23215069).

Author contributions

Ivan De Carlo 0000-0002-4066-8107
Conceptualization (lead), Data curation (lead), Formal analysis (lead), Investigation (lead), Methodology (lead), Software (equal), Writing – original draft (lead)

Davide Cipollini 0000-0003-4350-8691
Formal analysis (equal), Methodology (equal), Software (equal), Writing – original draft (equal)

Matteo Fretto 0000-0003-0053-6852
Methodology (equal)

Luca Boarino 0000-0002-1221-2591
Methodology (equal)

Andrea Lamberti 0000-0003-4100-9661
Resources (equal), Writing – review & editing (equal)

Gianluca Milano 0000-0002-1983-6516
Conceptualization (equal), Formal analysis (equal), Funding acquisition (lead), Methodology (equal), Resources (equal), Supervision (lead), Writing – original draft (equal)

References

[1] Lu W and Lieber C M 2007 Nanoelectronics from the bottom up *Nat. Mater.* **6** 841–50
[2] Dasgupta N P, Sun J, Liu C, Brittman S, Andrews S C, Lim J, Gao H, Yan R and Yang P 2014 25th anniversary article: semiconductor nanowires–synthesis, characterization and applications *Adv. Mater.* **26** 2137–84
[3] Comini E and Sberveglieri G 2010 Metal oxide nanowires as chemical sensors *Mater. Today* **13** 36–44
[4] Shen G, Chen P C, Ryu K and Zhou C 2009 Devices and chemical sensing applications of metal oxide nanowires *J. Mater. Chem.* **19** 828–39
[5] Cui Y, Wei Q, Park H and Lieber C M 2001 Nanowire nanosensors for highly sensitive and selective detection of biological and chemical species *Science* **293** 1289–92
[6] Meng J and Li Z 2020 Schottky-contacted nanowire sensors *Adv. Mater.* **32** 2000130
[7] Huang H, Liang B, Liu Z, Wang X, Chen D and Shen G 2012 Metal oxide nanowire transistors *J. Mater. Chem.* **22** 13428–45
[8] Heo Y, Tien L, Kwon Y, Norton D, Pearton S, Kang B and Ren F 2004 Depletion-mode ZnO nanowire field-effect transistor *Appl. Phys. Lett.* **85** 2274–6
[9] Fan Z, Wang D, Chang P C, Tseng W Y and Lu J G 2004 ZnO nanowire field-effect transistor and oxygen sensing property *Appl. Phys. Lett.* **85** 5923–5
[10] Chen D, Liu Z, Liang B, Wang X and Shen G 2012 Transparent metal oxide nanowire transistors *Nanoscale* **4** 3001–12
[11] Milano G, Porro S, Valov I and Ricciardi C 2019 Recent developments and perspectives for memristive devices based on metal oxide nanowires *Adv. Electron. Mater.* **5** 1800909
[12] Milano G, Luebben M, Ma Z, Dunin-Borkowski R, Boarino L, Pirri C F, Waser R, Ricciardi C and Valov I 2018 Self-limited single nanowire systems combining all-in-one memristive and neuromorphic functionalities *Nat. Commun.* **9** 5151
[13] Milano G, Boarino L, Valov I and Ricciardi C 2022 Memristive devices based on single ZnO nanowires–from material synthesis to neuromorphic functionalities *Semicond. Sci. Technol.* **37** 034002
[14] Milano G, D'Ortenzi L, Bejtka K, Ciubini B, Porro S, Boarino L and Ricciardi C 2021 Metal–insulator transition in single crystalline ZnO nanowires *Nanotechnology* **32** 185202
[15] Wei T Y, Yeh P H, Lu S Y and Wang Z L 2009 Gigantic enhancement in sensitivity using Schottky contacted nanowire nanosensor *J. Am. Chem. Soc.* **131** 17690–5
[16] Yeh P H, Li Z and Wang Z L 2009 Schottky-gated probe-free ZnO nanowire biosensor *Adv. Mater.* **21** 4975–8
[17] Milano G, Miranda E, Fretto M, Valov I and Ricciardi C 2022 Experimental and modeling study of metal–insulator interfaces to control the electronic transport in single nanowire memristive devices *ACS Appl. Mater. Interfaces* **14** 53027–37
[18] Milano G, Boarino L and Ricciardi C 2019 Junction properties of single ZnO nanowires with asymmetrical Pt and Cu contacts *Nanotechnology* **30** 244001
[19] Liu Y, Zhang Z, Hu Y, Jin C and Peng L M 2008 Quantitative fitting of nonlinear current–voltage curves and parameter retrieval of semiconducting nanowire, nanotube and nanoribbon devices *J. Nanosci. Nanotechnol.* **8** 252–8
[20] Zhang Z, Yao K, Liu Y, Jin C, Liang X, Chen Q and Peng L-M 2007 Quantitative analysis of current–voltage characteristics of semiconducting nanowires: decoupling of contact effects *Adv. Funct. Mater.* **17** 2478–89
[21] Padovani F A and Stratton R 1966 Field and thermionic-field emission in Schottky barriers *Solid-State Electron.* **9** 695–707
[22] Li S S 2006 Metal–semiconductor contacts *Semiconductor Physical Electronics* (Springer) pp 284–333
[23] Rhoderick E H 1982 Metal-semiconductor contacts *IEE Proc. I: Solid-State Electron Devices* **129** 1
[24] Crowell C and Rideout V 1969 Normalized thermionic-field (TF) emission in metal-semiconductor (Schottky) barriers *Solid-State Electron.* **12** 89–105
[25] Brent R P 2013 *Algorithms for Minimization Without Derivatives* (Courier Corporation)
[26] Lamberti A, Fontana M, Bianco S and Tresso E 2016 Flexible solid-state CuxO-based pseudo-supercapacitor by thermal oxidation of copper foils *Int. J. Hydrogen Energy* **41** 11700–8
[27] Yuan L, Wang Y, Mema R and Zhou G 2011 Driving force and growth mechanism for spontaneous oxide nanowire formation during the thermal oxidation of metals *Acta Metall.* **59** 2491–500
[28] Huang L, Yang S, Li T, Gu B, Du Y, Lu Y and Shi S Z 2004 Preparation of large-scale cupric oxide nanowires by thermal evaporation method *J. Cryst. Growth* **260** 130–5
[29] De Carlo I, Baudino L, Klapetek P, Serrapede M, Michieletti F, De Leo N, Pirri F, Boarino L, Lamberti A and Milano G 2023 Electrical and thermal conductivities of single Cu_xO nanowires *Nanomaterials* **13** 2822
[30] Lin Y F and Jian W B 2008 The impact of nanocontact on nanowire based nanoelectronics *Nano Lett.* **8** 3146–50
[31] Bercu B, Geng W, Simonetti O, Kostcheev S, Sartel C, Sallet V, Lérondel G, Molinari M, Giraudet L and Couteau C 2013 Characterizations of Ohmic and Schottky-behaving contacts of a single ZnO nanowire *Nanotechnology* **24** 415202
[32] Wu D, Zhang Q and Tao M 2006 LSDA+ U study of cupric oxide: electronic structure and native point defects *Phys. Rev. B* **73** 235206
[33] Singh B and Mehta B 2014 Relationship between nature of metal-oxide contacts and resistive switching properties of copper oxide thin film based devices *Thin Solid Films* **569** 35–43
[34] Tung R T 2014 The physics and chemistry of the Schottky barrier height *Appl. Phys. Rev.* **1** 011304
[35] Meng J, Lee C and Li Z 2024 Adjustment methods of Schottky barrier height in one-and two-dimensional semiconductor devices *Sci. Bull.* **69** 1342–52
[36] Liu X, Iocozzia J, Wang Y, Cui X, Chen Y and Zhao S 2017 Noble metal–metal oxide nanohybrids with tailored nanostructures for efficient solar energy conversion, photocatalysis and environmental remediation *Energy Environ. Sci.* **10** 402–34
[37] Hudait M, Venkateswarlu P and Krupanidhi S 2001 Electrical transport characteristics of Au/n-GaAs Schottky diodes on n-Ge at low temperatures *Solid-State Electron.* **45** 133–41
[38] Altındal Ş, Dökme İ, Bülbül M M, Yalçın N and Serin T 2006 The role of the interface insulator layer and interface states on the current-transport mechanism of Schottky diodes in wide temperature range *Microelectron. Eng.* **83** 499–505

[39] Yao J, Lin G, Du Z, Liang J, He H, Shen X and Fu Y 2021 Enhanced photoelectric properties of n-ZnO NWs/p-Si heterojunction LEDs by inserting an insulating MgO layer using sol–gel method *Electron. Mater. Lett.* **17** 355–61
[40] Zhang Z, Jin C, Liang X, Chen Q and Peng L M 2006 Current-voltage characteristics and parameter retrieval of semiconducting nanowires *Appl. Phys. Lett.* **88** 073102
[41] Wang W F, Cheng K Y, Wu M C and Hsieh K C 2018 Analyses of current-voltage characteristics using derivative methodology *Solid-State Electron.* **149** 15–22
[42] Korkut A 2018 New serial resistance equations: derivated from Cheungs' functions for the forward and reverse bias I *Microelectron. Eng.* **197** 45–52
[43] Wangyang P *et al* 2025 Advances in Schottky parameter extraction and applications *J. Mater. Sci. Technol.* **218** 317–35
[44] Rafiq M 2018 Carrier transport mechanisms in semiconductor nanostructures and devices *J. Semicond.* **39** 061002
[45] Lin T, Young S, Kung C, Chen H, Kao M, Chang M and Ou C R 2013 Variable-range hopping and thermal activation conduction of Y-doped ZnO nanocrystalline films *IEEE Trans. Nanotechnol.* **13** 425–30
[46] Motayed A, Davydov A V, Mohammad S and Melngailis J 2008 Experimental investigation of electron transport properties of gallium nitride nanowires *J. Appl. Phys.* **104** 024302
[47] Ma Y J, Zhou F, Lu L and Zhang Z 2004 Low-temperature transport properties of individual SnO2 nanowires *Solid State Commun.* **130** 313–6
[48] Shklovskii B I and Efros A L 2013 *Electronic Properties of Doped Semiconductors* vol 45 (Springer)
[49] Jeong Y K and Choi G M 1996 Nonstoichiometry and electrical conduction of CuO *J. Phys. Chem. Solids* **57** 81–84
[50] Florica C, Costas A, Boni A G, Negrea R, Ion L, Preda N, Pintilie L and Enculescu I 2015 Electrical properties of single CuO nanowires for device fabrication: diodes and field effect transistors *Appl. Phys. Lett.* **106** 223501
[51] Wu J, Yin B, Wu F, Myung Y and Banerjee P 2014 Charge transport in single CuO nanowires *Appl. Phys. Lett.* **105** 183506
[52] Jana R, Sil S, Dey A, Datta J and Ray P P 2018 Analysis of temperature dependent electrical performance of Al/CuO/ITO Schottky barrier diode and explanation of inhomogeneous barrier heights by double Gaussian distribution *AIP Adv.* **8** 125104
[53] Jin W, Mu X, Zhang K, Shang Z and Dai L 2018 Influence of interface inhomogeneity on the electrical transport mechanism of CdSe nanowire/Au Schottky junctions *Phys. Chem. Chem. Phys.* **20** 19932–7
[54] Lamberti A, Destro M, Bianco S, Quaglio M, Chiodoni A, Pirri C and Gerbaldi C 2012 Facile fabrication of cuprous oxide nanocomposite anode films for flexible Li-ion batteries via thermal oxidation *Electrochim. Acta.* **86** 323–9
[55] Virtanen P *et al* 2020 SciPy 1.0: fundamental algorithms for scientific computing in python *Nat. Methods* **17** 261–72
[56] De Carlo I, Cipollini D, Fretto M, Boarino L, Lamberti A and Milano G 2026 Quantitative analysis of current-voltage-temperature characteristics of metal-oxide nanowires *Zenodo* (https://doi.org/10.5281/zenodo.23214676)